Title

Voltage cycling as a dynamic operation mode for high temperature electrolysis solid oxide cells

Permalink

https://escholarship.org/uc/item/79t28724

Authors

Zhu, Zhikuan
Slomski, Heather S
Dzara, Michael J
et al.

Publication Date

2025-06-01

DOI

10.1016/j.jpowsour.2025.236958

Copyright Information

Voltage Cycling as a Dynamic Operation Mode for High Temperature Electrolysis Solid Oxide Cells

Zhikuan Zhu[1], Heather Slomski[2,3], Michael J. Dzara[2], Christopher A. Crain[4], Nicholas A. Strange[4], David Ginley[2], Brian P. Gorman[3], Sarah Shulda[2], and Michael C. Tucker[1*]

1. Energy Conversion Group, Lawrence Berkeley National Laboratory, Berkeley, CA 94720
2. National Renewable Energy Laboratory, Golden, CO 80401
3. Colorado School of Mines, Golden, CO 80401
4. Stanford Synchrotron Radiation Lightsource, SLAC National Accelerator Laboratory; Menlo Park, CA 94025

* Corresponding author: mctucker@lbl.gov

Abstract

Solid Oxide Electrolysis Cells (SOECs) have emerged as a promising technology for the efficient production of H_2 via high-temperature electrolysis. However, power input from dynamic energy sources remains a significant challenge for their long-term stability. It is important to analyze the tolerance of cells under dynamic operation conditions. This study focuses on evaluating the impact of voltage cycling on the performance and durability of electrode-supported SOECs. We explore the operational limits and degradation mechanisms of SOECs subjected to various voltage conditions and find that the cells have high tolerance for dynamic voltage. Voltage cycling between 1.3 V and 1.5 V for 9000 cycles does not damage the cell. Conversely, cycling to higher voltages (≥1.7 V) results in accelerated degradation. Advanced characterization is used to screen for various degradation modes post operation. Within the oxygen electrode, XRD and STEM EDS find compositional and phase evolution in all voltage cycled samples including increased decomposition of the air electrode resulting in cation migration. Microstructural analysis of the fuel electrode from nano-CT data shows minimal change throughout the sample set and no evidence of Ni migration, indicating the fuel electrode is stable and not impacted by cycling to higher voltages within the timeframe studied.

Keywords: solid oxide electrolysis; high temperature electrolysis; dynamic load; voltage cycling; microstructure characterization

1 Introduction

H_2 is an effective energy carrier [1-3]. Different methods can be used for H_2 production, including steam methane reforming, gasification and fermentation processes, biomass pyrolysis, photoelectrochemical water splitting, thermochemical water splitting, and electrolysis of water [4-8]. Among all these methods, solid oxide electrolysis cells (SOECs) represent a promising candidate that offers several advantages such as high efficiency, utilization of high temperature waste heat, flexible fuel input, low emission, high stability, and enhanced utilization of variable energy input [9-12].

During SOEC high temperature electrolysis (HTE) operation, electricity is used to split H_2O into H_2 and O_2, which results in zero emissions when using certain sources of electricity. The unique advantage of SOECs lies in their ability to operate at high temperatures, typically between 600 °C and 800 °C. This significantly enhances electrolysis efficiency relative to low-temperature electrolysis due to the more favorable thermodynamics and kinetics under high-temperature operation, and allows for utilization of high-quality waste heat from neighboring processes for production of steam [13-15]. SOECs can additionally co-electrolyze CO_2 and H_2O to produce syngas [16, 17]. Furthermore, the use of thermally-stable solid oxide materials facilitates SOEC integration with other high-temperature processes, for example utilizing surplus industrial waste heat to improve overall efficiency [12, 18], enhancing the potential for widespread applications. Challenges to decreasing the cost of HTE hydrogen production remain at the cell, stack, and system levels. The U.S. Department of Energy (DOE) consortium Hydrogen from Next-generation Electrolyzers of Water (H2NEW) aims to make HTE more durable, efficient, and affordable. The overarching approach is to couple cell fabrication and testing of button and large planar cells with detailed advanced characterization and multi-scale modeling to enhance understanding of critical performance and durability limitations.

Despite the HTE advantages, deployment of SOEC technology faces challenges, particularly in terms of operational stability under dynamic conditions. The future energy system is anticipated to have an increased share of intermittent electricity. Capture of excess, curtailed, or low-cost energy to produce hydrogen can contribute to the advancement of various sectors including transportation, industrial manufacturing, and residential heating [19, 20]. However, intermittent energy sources have large fluctuations based on time of day, dynamic weather, and instantaneous electricity cost [21-25]. Consequently, SOECs must be capable of withstanding these dynamic conditions without significant degradation to ensure long-term viability and integration into the energy system.

The complicated composition of SOECs paired with their layered structure results in a range of possible degradation mechanisms. The air electrode is prone to deterioration before cell testing due to high sintering temperatures with the exsolution and migration of Sr, Co/Fe spinel formation, and resultant formation of $SrZrO_3$ [26-29]. The barrier layer – electrolyte interface of the cell is prone to the buildup of resistive $SrZrO_3$, the formation of a solid solution, and is a known location of cell delamination [26, 28, 30, 31]. The fuel electrode can experience microstructural degradation, such as Ni redistribution, percolation changes, loss of active triple-phase boundary (TPB) length, and cracking in the YSZ, as well as issues from a variety of water contaminants such as Si and Al [32-34]. Here, a multi-scale multi-technique characterization approach is used to evaluate the full range of potential degradation phenomena and correlate the results to cycling condition.

In recent years, many studies have focused on stability of SOEC under dynamic conditions [35-40]. Voltage cycling (or power or current cycling) is frequently used to simulate the power supply from intermittent resources. These studies often focus on cycling between open circuit voltage (OCV) and near thermoneutral voltage (~1.3V) [41-44]. These voltage ranges present a relatively low stress on the cells, and the voltage cycling generally does not enhance degradation. For example, cells have been subjected to current-controlled switching between approximately OCV and 1.2V for 80,000 on/off cycles with 2 min cycle time [44], and for 1000 h with a 50 h dynamic load profile [36], without noticeable impact on the degradation behavior.

In this study, we extended the voltage range to include higher voltages, both to assess tolerance of SOECs to more aggressive or off-normal operating conditions, and to determine if high-voltage cycling might be used as an accelerated stress test (AST). All cells underwent thorough characterization to elucidate the impact of voltage cycling on cell degradation. By investigating the response of cells to various voltage conditions, including sustained high-voltage operation and rapid voltage cycling, a safe range of voltage was determined. This study supports the goals of utilizing dynamic electricity, developing accelerated stress tests for SOECs, and ultimately driving down the cost of hydrogen production.

2 Experimental Methods

2.1 Sample preparation and testing apparatus

Standard H2NEW SOEC button cells were designed and fabricated by Pacific Northwest National Laboratory (PNNL), which are comprised of a 20 µm coarse porous Ni current collection layer, a 500 µm coarse porous Ni-3-YSZ (3 mol. % Yttria-Stabilized Zirconia) support layer, a 20 µm fine porous Ni-8-YSZ (8 mol. % Yttria-Stabilized Zirconia) functional layer, a 7 µm dense 8-YSZ electrolyte, a 5 µm GDC ($Gd_{0.1}Ce_{0.9}O_{1.95}$) barrier layer, a 20 µm LSCF($La_{0.6}Sr_{0.4}Co_{0.2}Fe_{0.8}O_{3-x}$)-GDC electrode and a 20 µm LSCF current collection layer as shown in Figure 1a. The diameters of the Ni-YSZ substrate and LSCF-GDC electrode were 2.5 cm and 1.4 cm, respectively. The porous Ni layer was specifically designed to increase the bonding between the cell and current collector mesh.

Before loading the cell onto the alumina tube test rig as shown in Figure 1b, a platinum mesh was attached using platinum paste (Heraeus 6926) on the oxygen side of the cell, and nickel mesh was attached using NiO paste (provided by PNNL) on the hydrogen side. Both served as current collectors and were sintered simultaneously at 850 °C in air for 2 h. Platinum wires for current and voltage leads were attached on the meshes by spot welding. The cells were bonded to the test rig by alumina paste (Ceramabond 552, Aremco). A thermocouple was mounted near the top of the cell to monitor the temperature [45, 46]. All cells were reduced and tested at 750 °C. The oxygen side was exposed to ambient air. The hydrogen side was reduced with 10:90 H_2:N_2 (150 mL min^{-1}). After 3 h to 5 h reduction the open circuit voltage (OCV) became stable, and the H_2:N_2 ratio was gradually increased to 25:75 for 1h and 50:50 for 1h, followed by 97:3 H_2: H_2O. Stable OCV around 1.1 V was confirmed before further operation. One cell was cooled after this reduction protocol, and served as a baseline cell for characterization, herein referred to "as reduced". For all other cells, after overnight stabilization 50:50 H_2: H_2O was supplied to the hydrogen side by humidifying hydrogen gas (75 mL min^{-1}) in a heat-insulated water bubbler maintained at 82 °C.

Electrochemical impedance spectroscopy (EIS) at 1.3 V and current-voltage polarization (I-V) measurements were carried out at 750 °C, with ambient air (oxygen side) and 50:50 H_2: H_2O (hydrogen side) between each test phase to quantify cell degradation. Electrochemical measurements were conducted using a VMP3 multi-channel potentiostat with current booster (Biologic).

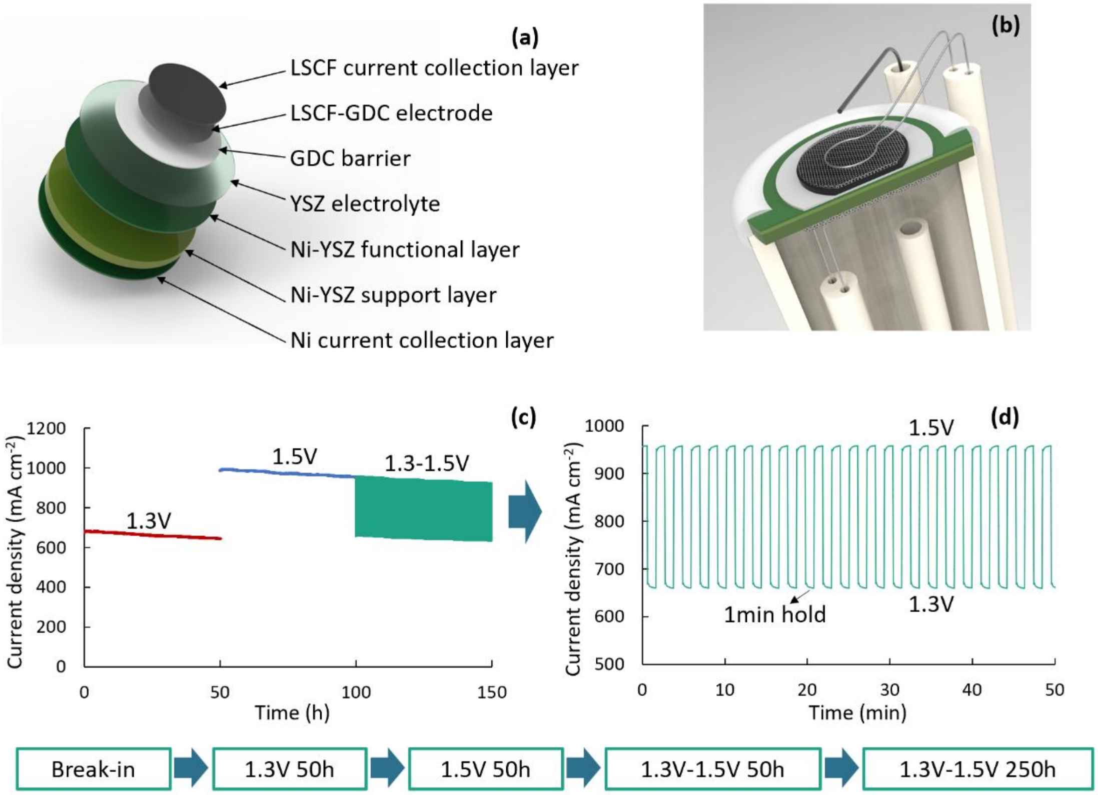

Fig 1. *Schematic of electrochemical experiment: (a) SOEC and (b) cell test set-up. Typical cell testing procedure: (c) Degradation in current density during stabilization (red), high voltage loading (blue), voltage cycling (green). (d) Zoom-in of current density change during voltage cycling with 1 min hold time.*

2.2 Cell operation protocol

Cells were tested to assess the impact of voltage cycling on performance and durability, including a baseline cell operated at a constant 1.3 V for 500 h and three cells subjected to cycling between 1.3 V and upper voltage limits of 1.5 V, 1.7 V, or 1.8 V. These cells are referred to throughout the text by their highest operating voltage.

Prior to variable-voltage operation, each cell was conditioned through a potentiostatic 150 h break-in period at 1.3 V to standardize their initial states, assess cell and seal quality, and ensure reliability in the subsequent testing phases. Following this initial conditioning, the cells were subjected to potentiostatic operation at their respective upper voltage limit for 50 h. These constant voltage steps confirmed reliability under sustained high-voltage conditions. This hold was eliminated for the 1.8 V cell to avoid dramatically exacerbating degradation before the cycling step.

Subsequently, they were cycled for 300 h between 1.3 V and the upper voltage limit, with a 1 min hold time at each voltage half-cycle. Preliminary work indicated that similar stability was obtained for hold times of 1, 5, 15, and 30 min, so 1 min was selected in order to accumulate many cycles during the testing period. The primary objective of this voltage cycling was to determine the cell endurance under dynamic voltage operation. I-V and EIS measurements were carried out before and after each test segment to monitor changes in performance. Current density at 1.3 V was recorded and used to compare degradation of all cells. Figure 1c and 1d present schematic representation of the cell operation procedure employed in our study. After voltage cycling, the cells were cooled with 97:3 H_2: H_2O flowing to prevent oxidation or liquid water condensation, carefully removed from the test rigs, and prepared for post-test characterization.

2.3 Cell characterization methods

STEM EDS

All cells were broken into cross section and polished using a JEOL ion beam cross section polisher. Scanning electron microscopy (SEM) and SEM EDS were collected on each sample to establish overall trends in the structural and chemical changes in each sample. SEM also confirmed that samples prepared for STEM analysis are representative of the changes observed in the bulk. Focused ion beam (FIB) preparation was conducted on an FEI Helios 600i SEM-FIB to produce lamellae for STEM, two lamellae were captured from the active layers of each sample to ensure that each interface is captured. Samples were then mounted to a copper TEM half grid and thinned using FIB thinning techniques. STEM micrographs and EDS spectral images were collected on a Thermo

Fisher Spectra 200 operating at 200 keV. STEM EDS spectral images were processed after collection with Brown-Powell ionization cross section quantification methods to reduce background and clarify regions of peak overlap between elemental signals.

Synchrotron-XRD

Stanford Synchrotron Radiation Lightsource (SSRL) beam line 2-1 was used for the synchrotron XRD measurements of each SOEC. Using an asymmetric reflection geometry, a 0.2 × 2 mm (vertical × horizontal) beam diffracted from SOECs with a 5 degree incident angle, resulting in a ~2.3 mm beam projection across the cells. The SOECs were prepared by removing remnants of the Ceramabond seal and securing on a magnetic mount with the oxygen electrode facing upwards (i.e. toward the incident beam). A robot-automated system was then utilized for the sample changes, alignment, and data collection. Data scans were acquired between 5 and 95 degrees two theta with a one-degree step size. A Pilatus 100K hybrid photon count detector was used for the collection of the 2D data at a sample distance of approximately 708 mm. This configuration yields a solid angle of ± 3°, providing significant overlap for signal averaging. Exposure times varied linearly between 7 and 10 seconds with increasing two-theta. The resulting 2D diffraction patterns were normalized to incident beam, stitched, and integrated using a python script developed for SSRL beam line 2-1. XRD data was qualitatively examined using Crystal Diffract and Rietveld refinements were performed using TOPAS Academic, version 7 [47].

Nano-CT

Microstructural characterization of the Ni-YSZ hydrogen electrode functional layer was performed using nano-CT. A cross-sectional region of interest (ROI) was first isolated from the center of a cell by fracturing with a razor blade, and then was adhered to a 1 mm stainless steel dowel using resin. Sample ROIs (Figure S3) were then shaped into pillars containing the YSZ electrolyte, the Ni-YSZ fuel electrode functional layer, and a portion of the Ni-YSZ fuel electrode support layer using an Oxford Instruments Laser Micromachining tool, yielding an ~50 - 100 μm diameter by ~200 μm length cylindrical ROI [48]. To ensure adequate X-ray transmission, fine thinning of sample pillars was performed using a 30 kV Ga ion beam in an FEI Helios 600i FIB, yielding a final diameter of ~ 8 – 12 μm at the YSZ/Ni-YSZ interface.

A Zeiss Xradia Ultra 810 equipped with a monochromatic Cr (5.4 keV) X-ray source was used for X-ray transmission image acquisition. The imaging field-of-view (FoV) contained 1,024 16.3 nm pixels, yielding dimensions of 16.7 x 16.7 μm. Imaging was performed over 180 ° in 0.1125 ° steps (1601 projections) using an exposure time of 70 seconds and a pixel binning factor of 2, resulting in a final pixel size of 32.6 nm in 2D grayscale images. Tomography alignment and reconstruction was performed with Zeiss software. Reconstructed 3D volumes were analyzed using Dragonfly 2022.2 (Comet Technologies Canada Inc.). A rectangular prism ROI was cropped from the internal volume of the tomogram, and then segmented into pore space, Ni, and YSZ phases using a 2D-Watershed algorithm. Watershed seeds were set based on the grayscale histogram (16-bit unsigned-short) and expanded using a 3D-Sobel transform of the grayscale data as a mask and treating the nearest 26 voxels as connected.

The resulting 3-phase segmentation was then converted to grayscale for microstructural analysis using a set of python scripts which have been described in detail elsewhere [49]. This analysis yields volumetric triple-phase boundary (TPB) length in terms of cumulative TPB length normalized to ROI volume estimated by labelling vertices as TPB points containing pore space, Ni, and YSZ in adjacent voxels, connecting the orthogonally adjacent TPB vertices, and then correcting for the resulting "staircase" over-estimation by upsampling the TPB pathways and smoothing with a 3D Gaussian kernel. Additional microstructural parameters calculated include phase fractions, connectivity, and tortuosity, interfacial surface area, phase size (estimated diameter by inscribed sphere method) and phase size diameter distribution.

3 Results and Discussion

3.1 Electrochemical testing results

The cells first underwent an initial break-in period (150-200 h at 1.3 V, approximately the thermoneutral voltage [50, 51]), until initial transients were complete and the current density degraded linearly. Then a high voltage test was conducted on each cell (50 h at the upper voltage limit), to evaluate the tolerance of the cells to high voltage and confirm that operation at the upper voltage limit would not cause catastrophic failure during cycling. Voltage above 1.8 V was suggested to be avoided by both theoretical calculation and the cell testing literature [52, 53], so 1.5 V and 1.7 V were selected as intermediate high voltage limits for testing here. This potentiostatic operation is shown in Figure 2. For the 1.5 V cell, the current density decreased by 38 mA cm^{-2} during the 50 h hold, similar to the 35 mA cm^{-2} drop observed at 1.3 V (Figure. 2a). Notably, at higher voltage the degradation rate was much faster. The 1.7 cell exhibited a substantial reduction in current density of 100 mA cm^{-2}.

EIS spectra before and after the voltage tolerance tests are shown in Figure 2b. No significant evolution of impedance was observed at 1.3 V and 1.5 V. In contrast, a marked increase in ohmic impedance was observed for 1.7 V, suggesting accelerated stress on the cell. Both potentiostatic operation and EIS affirm that the voltage range of 1.3 to 1.5 V remains within the safe threshold for cell testing, whereas elevating the voltage to 1.7 V or higher risks accelerated degradation. This is consistent with previous reports that operating at 1.6 V or 1.8 V increases the degradation rate [53, 54]. The differing reported safe upper limit may be due to variations in cell materials, structure, and test environment.

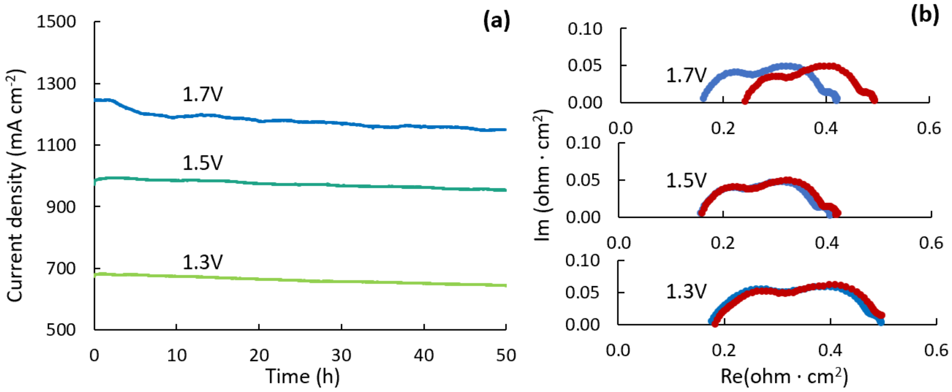

Fig 2. *Initial 50h constant voltage operation. (a) Current density degradation, and (b)EIS spectra before (blue) and after (red) 50 h testing.*

Voltage cycling for 300 h between 1.3 V and each upper voltage limit, with 1 min hold times, was aimed at evaluating endurance to dynamic voltage fluctuations. Tracking current density and impedance provided an assessment of degradation, Figure 2. A decline in current density at 1.3 V served as an indicator of cell degradation that could be easily compared for all cells, regardless of the upper voltage limit. Remarkably, all cells endured the full 500 h assessment, including 300 h of voltage cycling (9000 cycles), without any observable cell delamination, seal cracking, or decline in OCV.

For the baseline cell held at 1.3 V, there was a moderate drop in current density of 73 mA cm^{-2}. Similarly, the cell subjected to 1.3 to 1.5 V cycling exhibited a decrease of approximately 60 mA cm^{-2}. In contrast, the 1.7 V and 1.8 V cells showed decrease of 130 and 170 mA cm^{-2} at 1.3V, respectively, indicating a significantly higher rate of degradation due to the elevated voltage. EIS analysis corroborated these findings, with the 1.5 V cell showing similar small impedance change compared to the baseline cell. The 1.7 V and 1.8 V cells showed much larger ohmic and polarization impedance increases, further confirming that increased voltage correlates with accelerated degradation rate. For example, the ohmic and polarization increases were 0.014 and 0.048 Ohm cm^2 after the 1.3V hold, and 0.227 and 0.071 Ohm cm^2 after the 1.3-1.8V cycling, respectively (Figure 3).

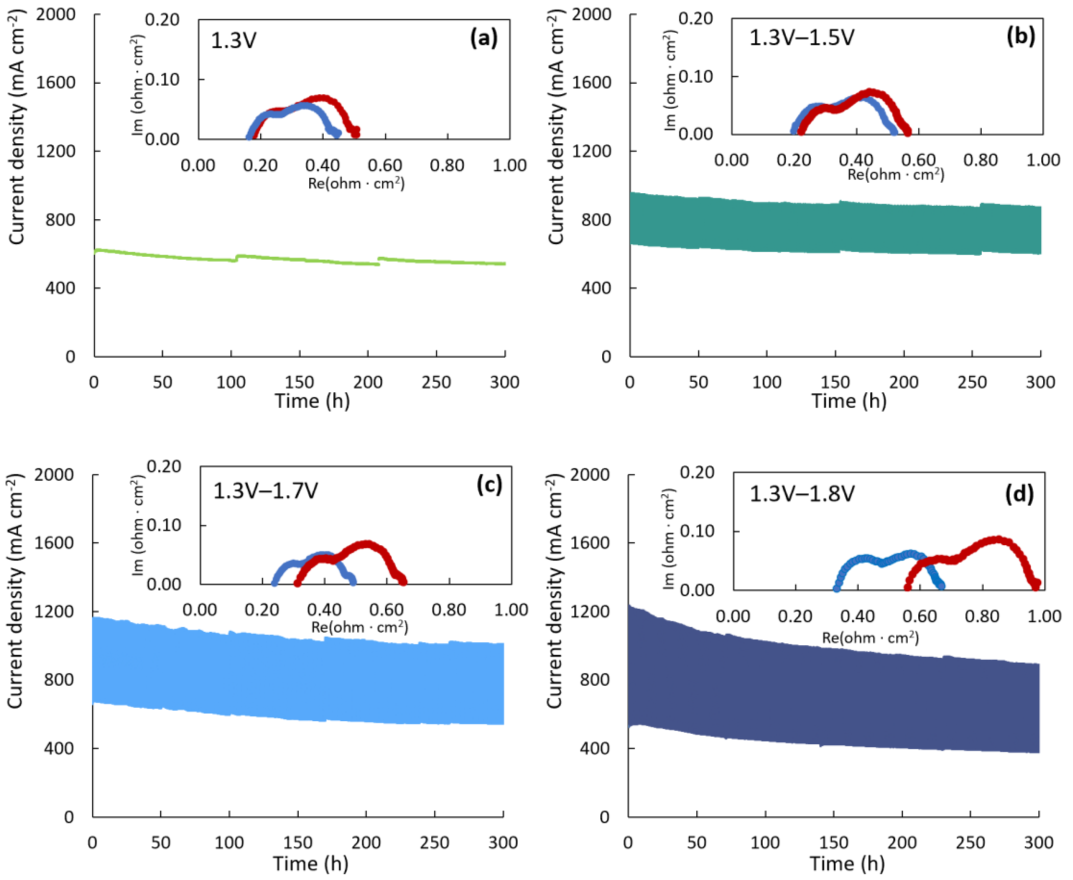

Fig 3. *Degradation of current density, EIS spectra of cells before (blue) and after (red) 300 h operation at. (a) baseline 1.3V, (b) 1.3-1.5 V, (c) 1.3-1.7 V, and (d) 1.3-1.8 V.*

3.2 Microstructural characterization results

The oxygen electrode and barrier layer were analyzed with STEM EDS and X-ray diffraction, focusing on cation migration and phase evolution. The electrolyte was imaged with STEM, focusing on nano-void formation. The Ni-YSZ fuel electrode was analyzed with nano-CT, focusing on evolution of triple-phase boundary (TPB) length and conduction path connectivity.

3.2.1 Oxygen electrode and barrier layer

Microscopy

STEM EDS is used to spatially map chemical and microstructural changes in high resolution and has been used to examine many degradation symptoms including: Sr, Co, Fe, and La exsolution and migration from the air electrode through the barrier layer, densification at interfaces, and Si and Al contamination [26, 29, 55-63]. STEM EDS was collected on each sample to determine the degradation mechanisms that are present.

Sr migration through the GDC barrier layer is exacerbated by cycling to high voltages. STEM-EDS mapping of the as-reduced sample illustrates minor Sr migration resulting in small clusters through the GDC barrier layer, Figure 4a. This indicates that during the cell manufacturing and high operating temperatures, minor Sr exsolution from LSCF occurs, which diffuses out of the oxygen electrode and through the barrier layer towards the electrolyte [55, 64]. After 500 hours of 1.3 V hold, there is not a significant change in the Sr distribution and there is no further progression across the barrier layer, indicating little change in the cell from the potentiostatic operation within that timeframe. With 1.3 - 1.5 V cycling, larger quantities of Sr have accumulated at the barrier/electrolyte interface, with Sr clusters observable at the electrolyte. Similarly, the 1.3 - 1.7 V cycle has Sr clusters that have migrated to the interface and build up at the electrolyte. The 1.3 - 1.7 V cycle sample shows a cluster of Y within the YSZ that has been seen in previous samples produced by our source and is noted as an effect of manufacturing and is not indicated to be a result of voltage cycling. The 1.3 - 1.8 V cycled cell has both mobile clusters of Sr in the barrier layer and notable Sr clusters in a small area of porosity in the YSZ indicating progression past the interface and trace $SrZrO_3$ formation. Overall, cycling at all voltages resulted in increased Sr migration into and through the GDC barrier layer indicating electrode degradation. However, the extent of migration is not directly correlated with the cycling voltage and thus is not considered a direct cause of observed performance loss. The migration of Sr and formation of $SrZrO_3$ is a well-documented degradation mechanism in both long term and short-term cell testing studies [26, 55, 56, 65]. Pairing the STEM EDS results with XRD (discussed below) indicates that any $SrZrO_3$ present within the 1.3 - 1.8 V cycle cell is a volume so small that it is not detectable in XRD and therefore also is not considered to be a primary degradation mechanism in this study.

Further STEM-EDS of the GDC/YSZ interface indicates the migration of small clusters of Co and Fe accompanying the Sr, from the decomposition of LSCF (Figure 4b). Traces of these elements are seen in the as-reduced sample in the GDC and in the 500-hr 1.3V hold sample. More extensive migration is observed for the voltage-cycled samples.

In the 1.3-1.5V cycle sample, Fe is seen with some of the Sr clusters (overlapping Fe and Sr signal appears sky blue) at the interface and trace amounts of Co migrated through the GDC. As voltage cycling progresses to the 1.3-1.7V and 1.3-1.8V samples, Co and Fe are seen migrating to, and collecting at, the YSZ electrolyte. Co and Fe migration through GDC appears to be associated with higher voltages when compared to 1.3V operation for the same length of time. This result is notable as migration of Co and Fe through the barrier is a phenomenon not commonly observed in cell testing at typical (lower) voltage limits. Co migration through the barrier layer has been observed in some previous studies, however, it has not been associated with mobile Fe clusters as seen in the samples here [57-59]. Increasing presence of Co and Fe within the GDC and at the electrolyte corresponds to XRD identification of Co-Fe spinel species the higher voltage cycled cells (described below). This is consistent with voltage-induced changes in the mechanisms of LSCF decomposition and indicates a contributor to degradation of intended phases within the cell.

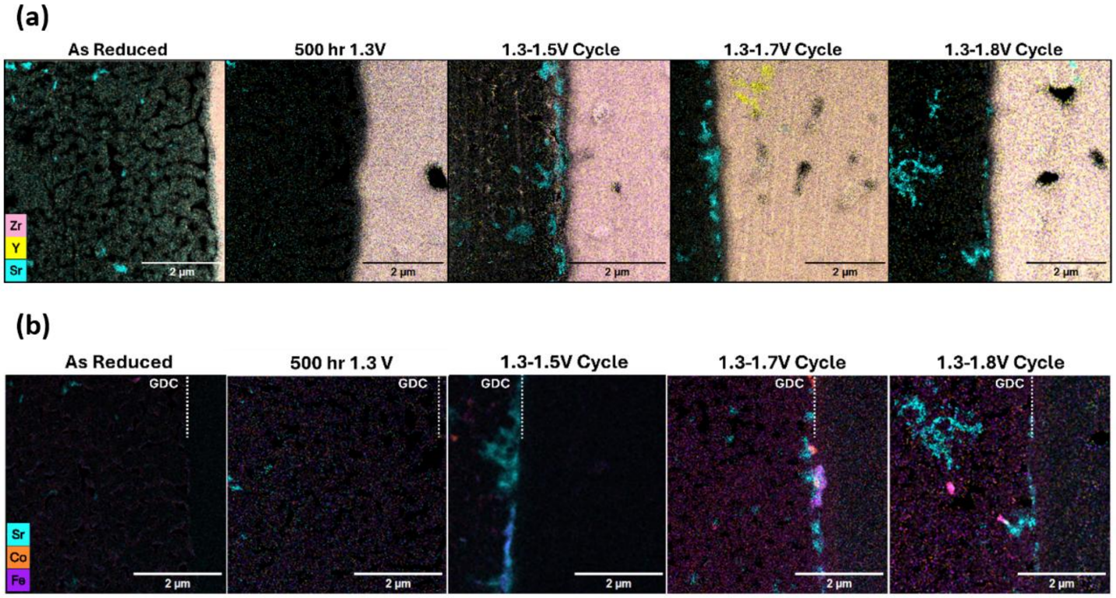

Fig 4. *Sr and Y segregation: (a) STEM EDS mapping of Sr (blue), Y (yellow), and Zr (pink) signal at the GDC/YSZ interface illustrating the progression of Sr to the GDC/YSZ interface from voltage cycling. Note that the As-Reduced sample and the 1.3-1.5V cycled sample have more EDS signal background and YSZ florescence than the others, creating the appearance of pink grains and pores that should be ignored.*

Sr, Co, and Fe segregation: (b) STEM EDS mapping of Sr (cyan), Co (orange), and Fe (purple) signal illustrate Fe and Co migrating alongside mobile Sr and accumulating at the GDC/YSZ interface (marked with dashed white line). Regions of Fe-Sr appear sky blue, Co-Fe appear pink and fuchsia depending on the elemental ratio, and areas of Sr-Co-Fe appear bright purple.

As seen in Figure 5, the formation of an interaction layer between the GDC and YSZ is observed with higher-magnification STEM-EDS. An increase in atomic number and modification of the grain structure are observed using high angle annular dark field (HAADF) STEM imaging (Figure 5a), appearing as a lighter region between the porous GDC and dense YSZ layers. This layer corresponds to Ce and Gd diffusion into the YSZ as observed in the EDS maps (Figure 5b). No notable changes in the interdiffusion layer is observed, suggesting that the Ce and Gd layers form during cell processing and there is little or no additional migration as a result of cell operation. This observation is consistent with previous work where an interdiffusion layer has been documented to form between YSZ and GDC during sintering [29]. This phenomenon warrants attention, as previous studies have found that this layer may degrade electrochemical performance and mechanical strength [66, 67].

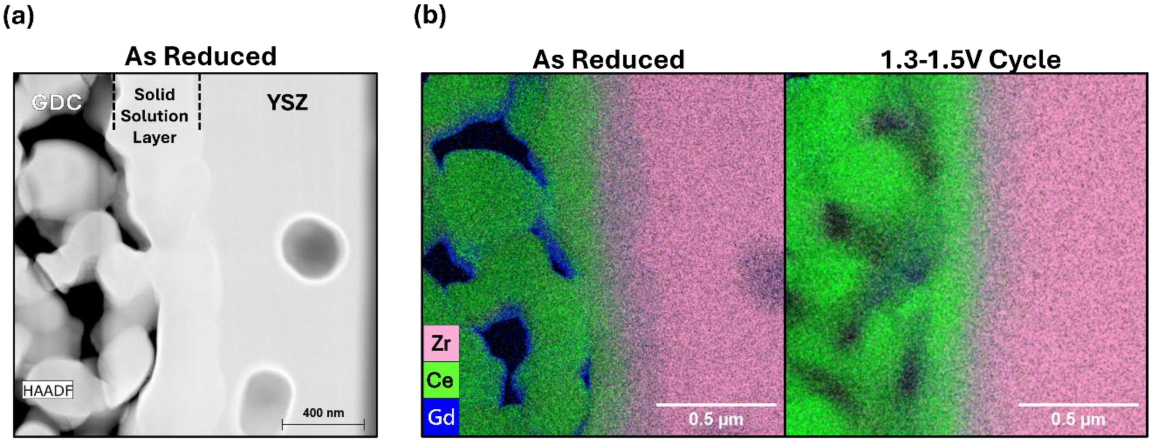

Fig 5. *GDC-YSZ reaction layer. (a) HAADF STEM imaging indicating a distinct interdiffusion layer at the YSZ/GDC interface. (b) STEM EDS mapping of Zr(pink), Ce(lime), and Gd(dark blue) of the as reduced and 1.3-1.5V cycled samples indicating no significant change in the thickness of the interdiffusion layer after testing.*

Several other known degradation mechanisms were evaluated and ruled out through a thorough multi-scale electron microscopy examination of the cells (Figures 4-8, SI Figures S2 and S3) including: bulk $SrZrO_3$ formation [26]; LaZrO formation [68]; cell poisoning from known contaminants Al, Si, Na, B, etc. [69, 70], and Ni agglomeration. Additionally, the layer interfaces were evaluated with SEM-EDS and no indication of contamination, densification, or other changes that would cause a degradation in performance were observed (SI Figure S2).

Diffraction

In the present configuration, the XRD data are largely sensitive to bulk crystalline structural changes across a significantly larger material volume relative to the STEM data and are used to derive global structural changes. XRD characterization of the oxygen electrode of each SOEC was used to determine modifications to the intended structural phases and any secondary phase formation. XRD data from all SOECs are displayed in Figure 6. As expected, the primary structural components including the target rhombohedral-LSCF structure, GDC, Pt (contact paste) and YSZ were observed (Ni is too deep to be observed at this combination of energy and incidence angle). For the as-reduced sample, a cubic-LSCF structure (i.e., Sr-rich) and a minor additional cobalt ferrite spinel structure is also identified, which is presumed to exsolve from the LSCF anode during cell processing or the reduction step. The presence of the cobalt ferrite spinel implies the existence of "free" A-site cations (presumably Sr as observed in TEM) in the absence of a secondary phase that breaks the ABO_3 perovskite stoichiometry. However, we suspect that the crystallite or population sizes are too small to be detected with XRD.

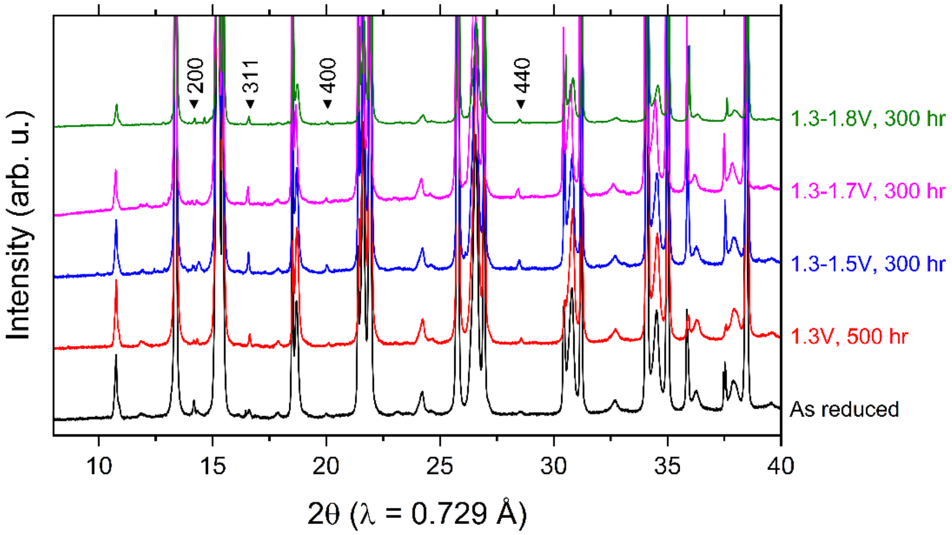

Fig 6. *XRD analysis. Synchrotron XRD traces from all SOECs before operation (as reduced) and after potentiostatic or voltage cycling operation. The reflections and associated Miller indices from the cobalt ferrite spinel are identified by triangles. Unlabeled peaks are associated with desired structures of SOEC layers.*

Rietveld refinements of the XRD data were performed in order to quantify changes to the SOEC component structures during cell operation (see Figures S5-9). Quantitatively, the weight percent of the cobalt ferrite spinel increases only slightly from the as-fired or as-reduced states, Figure 7. Interestingly, the weight percent of the Sr-rich cubic LSCF secondary phase is at its highest in the pre-operation stages, and steadily decreases as a function of maximum voltage. Despite minimal change in the concentration of spinel, the lattice parameter appears to increase as a function of maximum potential in the voltage cycling series. Because the lattice parameter of a cobalt ferrite spinel does not follow a linear relationship with cation substitution due to the complexities of the pure Co or Fe spinel structures (normal vs. inverse spinel, low vs. high spin, composition distributions), an assignment of the exact spinel composition is not possible with the existing dataset. However, using a literature-sourced estimation of the relationship between lattice parameter and composition (see Figure S13), we show that the maximum potential of the voltage cycling influences the observed lattice parameter which is likely associated with the spinel composition (and associated cation reduction potentials). Using the available literature data relating spinel lattice parameter to composition, these XRD results indicate a range of spinel compositions from 0.668-1.751 moles of cobalt per mole of spinel. Despite the minimal degradation observed in the electrochemistry, the composition of the spinel may influence oxide and electronic conductivities through the oxygen electrode. Exsolution of the b-site cations from LSCF could play a role in the degradation of current density seen in the electrochemical analysis and is likely linked to the exsolution of Sr illustrated in the STEM EDS findings.

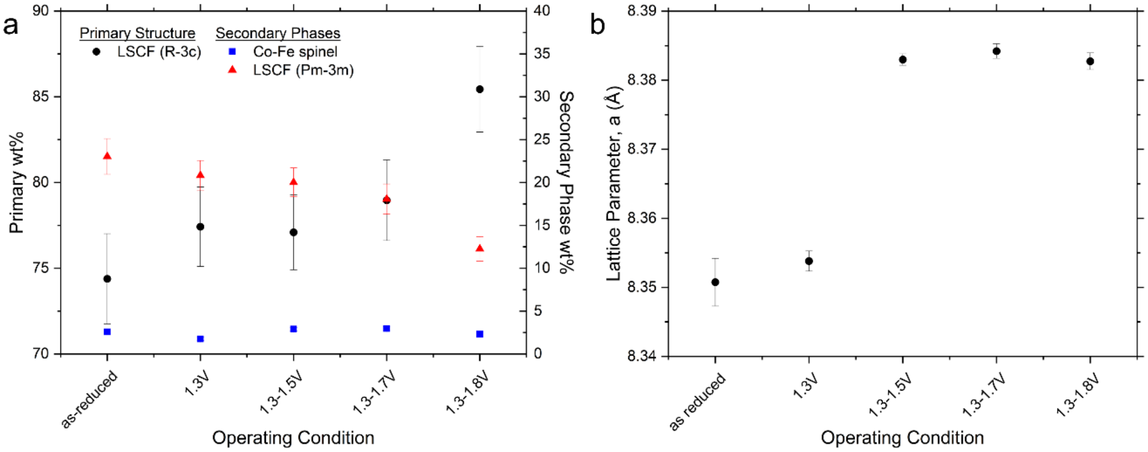

Fig 7. *Summary of Rietveld analysis. a) Weight percents of oxygen electrode structural phases and b) cobalt ferrite lattice parameter as a function of HTE operating condition.*

Overall, gradual changes in Sr, Co, and Fe cation migration within the cells can be associated with voltage cycling, especially to higher voltages, and is reflected in STEM EDS and XRD analyses. LSCF cation migration in the oxygen electrode, including migration of Sr to the GDC/YSZ interface and formation of $SrZrO_3$, is observed under normal testing conditions and is accelerated by cycling to higher voltages. The migration of Co and Fe with Sr across the barrier layer is a unique degradation symptom only observed in the voltage cycled samples. This indicates that high voltage cycling forms multiple decomposition phases differing from potentiostatic operation, the effects of which are not yet fully understood, but presumably contribute to the observed electrochemical degradation.

3.2.2 Electrolyte

The formation of voids and cracks throughout the YSZ electrolyte is a phenomenon that has been previously noted in accelerated aging studies at high voltages, and in long term aging studies [60-63]. STEM imaging was used to investigate if this degradation mechanism occurs here. Micro-voids are formed in the YSZ electrolyte of the 1.3 - 1.7 V cycled cell, Figure 8a. Cells cycled to 1.8V and 1.9V typically also display void formation (SI Figure. S14). As the voids will reduce the in-plane area for ion transport, their formation is expected to increase ohmic impedance, consistent with the results above. Therefore, void formation is thought to be a significant degradation mode for cells exposed to higher voltages.

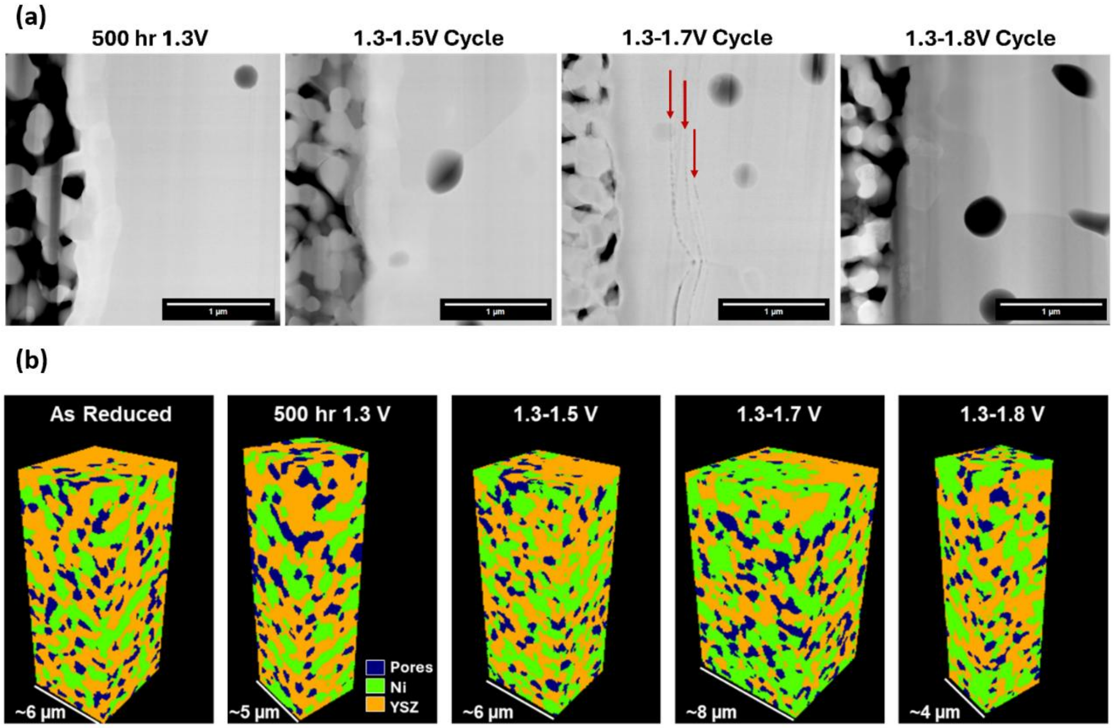

Fig 8. *Nano-void formation in YSZ electrolyte: (a) STEM HAADF imaging of the GDC/YSZ interface reveals cracking (marked with red arrows) in the electrolyte of the 1.3-1.7V cycle sample and cells cycled to higher voltage (shown in SI Figure. S14). Fuel electrode structure: (b) 3D segmented volumes of an ROI from within the fuel electrode functional layer are displayed for each sample at the same scale, with the interface nearest the YSZ electrolyte oriented at the top of the image.*

3.2.3 Fuel electrode

Characterization of the Ni-YSZ fuel electrode functional layer was performed with a lab-source nano-CT in order to identify any loss in volumetric TPB length or decreases in conductive pathway connectivity that may lead to decreased cell current density and/or increased impedance. Within the literature on SOEC degradation, Ni migration, Ni coarsening, and Ni detachment from YSZ are of particular concern [32, 33, 71]. Generally, 3D Ni-YSZ microstructural data has been obtained with synchrotron source nano-CT and other synchrotron techniques, or FIB serial sectioning, including several studies showing Ni redistribution in cells operated for multiple thousands of hours, and/or at high (>1 A/cm^2) current densities, elevated temperatures, or at the steam inlet/outlet of a rectangular cell [72-78]. A comprehensive link between operating conditions and Ni redistribution is not yet available across the literature due to differences in hydrogen electrode microstructure which likely convolutes the relationship between cell testing and the onset and extent of Ni redistribution.

The segmented 3D nano-CT data representative of each cell is presented in Figure 8b, while key microstructural properties calculated from the segmented volumes and their variation across the sample set are presented in Table 1. Visual inspection of the segmented volumes does not reveal any significant differences in the spatial distribution of Ni, YSZ, or pore phases, or any evidence for Ni detachment which can be identified by characteristic narrow, arc-shaped pores between Ni and YSZ. Generally, the microstructural values are similar to the literature, although caution must be applied in comparing values of TPB density which are dependent on the resolution of the measurement [79]. The phase fractions and average phase size are typical for the field, although the pore fraction is among the lower values reported, which may also lead to TPB connectivity values below 80%. Little to no change in the quantified microstructure is observed, with no appreciable decrease in volumetric TPB length or connectivity, as all volumetric TPB lengths fall within ±9 % of the average value across the dataset. In the context of the literature, decreases in TPB density of 25 – 50 % are reported when evidence of Ni redistribution is present [72, 73, 76, 77]. Minimal change in the Ni-YSZ interfacial area also confirms the lack of evidence for Ni-YSZ detachment, while consistent phase sizes suggest no Ni coarsening occurred.

Literature has shown that for commercially available Ni-YSZ hydrogen electrodes, microstructure heterogeneity may be present at a scale spanning tens to hundreds of microns [78]. To account for this possibility in cells studied in this work, two separate volumes were analyzed and an average of the microstructural outputs is displayed in Table 1 for the extrema (the as-reduced, and 1.3 – 1.8 V samples). The variation across the dataset in microstructural parameters is generally very similar to the degree of variation in the two distinct volumes analyzed for the as-reduced sample, suggesting that the slight variation across samples in Table 1 are only due to measurement error or sample heterogeneity. Phase size distribution and phase fraction variation were evaluated as a function of depth to determine if Ni coarsening and/or migration towards or away from the electrolyte interface occurred (Figure S4). Again, little to no change in microstructure is revealed, confirming that no Ni coarsening or migration occurs. The lack of any clear trend in volumetric TPB length, phase connectivity, and phase size and depth distribution indicate that the fuel electrode functional layer remains stable throughout the potentiostatic and voltage cycling tests and is unlikely to be the primary contributor to the increased impedance and current loss observed in Figure 3. Other studies have found that over-polarization from high voltages may play a role in preventing this degradation mode [80], whereas others point to the microstructure of the fuel electrode itself and the purity of the inlet gas in playing a crucial role [71]. While the reason behind the lack of Ni-migration cannot be directly determined in this study, it can be ruled out as a cause of the observed performance loss.

Table 1: Fuel electrode functional layer microstructural parameters

Property	As Reduced	500 hr 1.3 V	1.3-1.5 V	1.3-1.7 V	1.3-1.8 V	Standard Deviation
Volumetric TPB (µm/µm^3)	3.3	3.1	3.3	3.6	3.7	± 0.31
TPB connectivity (%)	76	79	73	71	81	± 4.9
Ni fraction (%)	32	32	36	37	34	± 2.4
Ni phase size (µm)	0.49	0.56	0.51	0.51	0.50	± 0.026
Ni connectivity (%)	99.3	99.4	99.6	99.0	99.1	± 0.280
YSZ fraction (%)	53	50	50	47	50	± 2.2
YSZ phase size (µm)	0.56	0.56	0.52	0.52	0.52	± 0.024
YSZ connectivity (%)	99.9	99.9	99.9	99.9	99.9	± 0.0413
Pore fraction (%)	15	17	13	16	16	± 1.3

Pore phase size (µm)	0.38	0.42	0.36	0.40	0.40	± 0.021
Pore connectivity (%)	86	89	83	83	92	± 3.8
Ni-YSZ specific interfacial area ($µm^2$/ $µm^3$)	2.0	1.8	2.2	2.3	2.1	± 0.20
Ni-Pore specific interfacial area ($µm^2$/ $µm^3$)	0.65	0.55	0.66	0.75	0.63	± 0.082
YSZ-Pore specific interfacial area ($µm^2$/ $µm^3$)	0.87	0.91	0.79	0.87	0.87	± 0.11
Volume analyzed ($µm^3$)	847	338	472	823	530	N/A

4 Conclusions

This study investigated the performance and durability of electrode-supported SOECs under dynamic voltage conditions. After break-in, the cells underwent high-voltage tolerance and voltage cycling tests to evaluate their resilience and operational stability. Operating the cells under fluctuating voltage ranging from 1.3 to 1.5 V does not accelerate degradation. In contrast, subjecting the cells to higher voltages of 1.7 V and above resulted in significant performance degradation, marked by a pronounced drop in current density and increased ohmic and polarization impedances. Nevertheless, all cells survived the comprehensive 500 h test regimen without physical failure such as delamination or seal cracking, leading to OCV stability.

All cells tested under dynamic cycling show increased cation segregation and migration into the barrier layer, observed with STEM EDS analysis. Increased Sr, Co, and Fe migration across the barrier layer and accumulation at the GDC/YSZ interface are observed. Clusters of Sr are present in the YSZ after cycling at 1.3-1.8V. Formation of Co-Fe-oxide spinel phase is confirmed with XRD. Although the XRD shows minute changes in spinel weight percent with voltage cycling, the TEM data shows that it migrates into the electrolyte, suggesting a possible increase. Further, the higher maximum voltages appear to influence the composition of the spinel. Cells with cycling to 1.7V or higher typically show void formation within the electrolyte. In contrast, microstructural characterization of the fuel electrode functional layer by nano-CT revealed essentially no change, indicating that the Ni-YSZ functional layer is stable when cycled to higher voltages within the timeframe of this study, and at the current densities achieved. No other significant changes are detected, suggesting that the electrochemical degradation arises primarily from the observed LSCF decomposition and void formation.

This study explored degradation under dynamic voltage conditions, offering valuable guidance for the optimization of SOEC operation in practical applications. High voltage loading during dynamic operation should be avoided. Specifically, intermittent operation well above the thermoneutral voltage was explored systematically, and upper voltage limits associated with safe operation (1.5 V) and accelerated degradation (1.7 V and above) were identified.

5 Declaration of competing interest

The authors declare that they have no known competing financial interests or personal relationships that could have appeared to influence the work reported in this paper.

6 CRediT authorship contribution statement

Zhikuan Zhu: Methodology, Investigation, Data curation, Visualization, Writing - original draft. **Heather Slomski:** Investigation, Data curation, Writing - original draft. **Michael J. Dzara:** Investigation, Data curation, Visualization, Writing - original draft. **Christopher A. Crain:** Investigation, Data curation, Validation. **Nicholas A. Strange:** Investigation, Data curation, Validation, Writing - original draft. **David Ginley:** Investigation, Validation, Resources. **Brian P. Gorman:** Investigation, Validation, Resources. **Sarah Shulda:** Investigation, Validation, Resources. **Michael C. Tucker:** Conceptualization, Methodology, Investigation, Writing - original draft, Writing - review and editing, Resources, Supervision, Funding acquisition.

7 Acknowledgements

The authors thank Martha Welander for assistance in establishing this study. This material is based upon work supported by the U.S. Department of Energy's Office of Energy Efficiency and Renewable Energy (EERE) under the H_2 from the Next-generation Electrolyzers of Water (H2NEW) consortium for funding under Contract Number DE-AC02-05CH11231. This document was prepared as an account of work sponsored by the United States Government. While this document is believed to contain correct information, neither the United States Government nor any agency thereof, nor the Regents of the University of California, nor any of their employees, makes any warranty, express or implied, or assumes any legal responsibility for the accuracy, completeness, or usefulness of any information, apparatus, product, or process disclosed, or represents that its use would not infringe privately owned rights. Reference herein to any specific commercial product, process, or service by its trade name, trademark, manufacturer, or otherwise, does not necessarily constitute or imply its endorsement, recommendation, or favoring by the United States Government or any agency thereof, or the Regents of the University of California. The views and opinions of authors expressed herein do not necessarily state or reflect those of the United States Government or any agency thereof or the Regents of the University of California. This manuscript has been authored by an author at Lawrence Berkeley National Laboratory under Contract No. DE-AC02-05CH11231 with the U.S. Department of Energy. The U.S. Government retains, and the publisher, by accepting the article for publication, acknowledges, that the U.S. Government retains a non-exclusive, paid-up, irrevocable, world-wide license to publish or reproduce the published form of this manuscript, or allow others to do so, for U.S. Government purposes. This work was authored in part by the National Renewable Energy Laboratory, operated by Alliance for Sustainable Energy, LLC, for the U.S. Department of Energy (DOE) under Contract No. DE-AC36-08GO28308. Use of the Stanford Synchrotron Radiation Lightsource, SLAC National Accelerator Laboratory, is supported by the U.S. Department of Energy, Office of Science, Office of Basic Energy Sciences under Contract No. DE-AC02-76SF00515.

8 References

[1] Abe JO, Popoola A, Ajenifuja E, Popoola OM. Hydrogen energy, economy and storage: Review and recommendation. International journal of hydrogen energy. 2019;44:15072-86.

[2] Yue M, Lambert H, Pahon E, Roche R, Jemei S, Hissel D. Hydrogen energy systems: A critical review of technologies, applications, trends and challenges. Renewable and Sustainable Energy Reviews. 2021;146:111180.

[3] Rosen MA, Koohi-Fayegh S. The prospects for hydrogen as an energy carrier: an overview of hydrogen energy and hydrogen energy systems. Energy, Ecology and Environment. 2016;1:10-29.

[4] Posdziech O, Schwarze K, Brabandt J. Efficient hydrogen production for industry and electricity storage via high-temperature electrolysis. International Journal of Hydrogen Energy. 2019;44:19089-101.

[5] Sazali N. Emerging technologies by hydrogen: A review. International Journal of Hydrogen Energy. 2020;45:18753-71.

[6] Dawood F, Anda M, Shafiullah G. Hydrogen production for energy: An overview. International Journal of Hydrogen Energy. 2020;45:3847-69.

[7] Abdalla AM, Hossain S, Nisfindy OB, Azad AT, Dawood M, Azad AK. Hydrogen production, storage, transportation and key challenges with applications: A review. Energy conversion and management. 2018;165:602-27.

[8] Chau K, Djire A, Khan F. Review and analysis of the hydrogen production technologies from a safety perspective. International Journal of Hydrogen Energy. 2022;47:13990-4007.

[9] Tucker MC. Progress in metal-supported solid oxide electrolysis cells: A review. International journal of hydrogen energy. 2020;45:24203-18.

[10] Wendel C, Kazempoor P, Braun R. Novel electrical energy storage system based on reversible solid oxide cells: System design and operating conditions. Journal of Power Sources. 2015;276:133-44.

[11] Laguna-Bercero MA. Recent advances in high temperature electrolysis using solid oxide fuel cells: A review. Journal of Power sources. 2012;203:4-16.

[12] Ni M, Leung MK, Leung DY. Technological development of hydrogen production by solid oxide electrolyzer cell (SOEC). International journal of hydrogen energy. 2008;33:2337-54.

[13] Ferrero D, Lanzini A, Santarelli M, Leone P. A comparative assessment on hydrogen production from low-and high-temperature electrolysis. International journal of hydrogen energy. 2013;38:3523-36.

[14] Udagawa J, Aguiar P, Brandon N. Hydrogen production through steam electrolysis: Model-based steady state performance of a cathode-supported intermediate temperature solid oxide electrolysis cell. Journal of Power Sources. 2007;166:127-36.

[15] Herring JS, O'Brien JE, Stoots CM, Hawkes G, Hartvigsen JJ, Shahnam M. Progress in high-temperature electrolysis for hydrogen production using planar SOFC technology. International Journal of Hydrogen Energy. 2007;32:440-50.

[16] Schiller G, Ansar A, Lang M, Patz O. High temperature water electrolysis using metal supported solid oxide electrolyser cells (SOEC). Journal of Applied Electrochemistry. 2009;39:293-301.

[17] Dincer I, Acar C. Innovation in hydrogen production. International Journal of Hydrogen Energy. 2017;42:14843-64.

[18] Mahato N, Banerjee A, Gupta A, Omar S, Balani K. Progress in material selection for solid oxide fuel cell technology: A review. Progress in Materials Science. 2015;72:141-337.

[19] Chi J, Yu H. Water electrolysis based on renewable energy for hydrogen production. Chinese Journal of Catalysis. 2018;39:390-4.

[20] Hauch A, Küngas R, Blennow P, Hansen AB, Hansen JB, Mathiesen BV, Mogensen MB. Recent advances in solid oxide cell technology for electrolysis. Science. 2020;370:eaba6118.

[21] Petipas F, Brisse A, Bouallou C. Model-based behaviour of a high temperature electrolyser system operated at various loads. Journal of Power Sources. 2013;239:584-95.

[22] Cai Q, Adjiman CS, Brandon NP. Optimal control strategies for hydrogen production when coupling solid oxide electrolysers with intermittent renewable energies. Journal of Power Sources. 2014;268:212-24.

[23] Sanz-Bermejo J, Muñoz-Antón J, Gonzalez-Aguilar J, Romero M. Part load operation of a solid oxide electrolysis system for integration with renewable energy sources. International Journal of Hydrogen Energy. 2015;40:8291-303.

[24] Jensen SH, Larsen PH, Mogensen M. Hydrogen and synthetic fuel production from renewable energy sources. International Journal of Hydrogen Energy. 2007;32:3253-7.

[25] Liu H, Høgh J, Blennow P, Sun X, Zong Y, Chen M. Assessing fluctuating wind to hydrogen production via long-term testing of solid oxide electrolysis stacks. Applied Energy. 2024;361:122938.

[26] Lu Z, Darvish S, Hardy J, Templeton J, Stevenson J, Zhong Y. SrZrO3 formation at the interlayer/electrolyte interface during (La1-xSrx) 1-δCo1-yFeyO3 cathode sintering. Journal of The Electrochemical Society. 2017;164:F3097.

[27] Jiang SP. Development of lanthanum strontium cobalt ferrite perovskite electrodes of solid oxide fuel cells – A review. International Journal of Hydrogen Energy. 2019;44:7448-93.

[28] Pan Z, Liu Q, Lyu R, Li P, Chan SH. Effect of La0.6Sr0.4Co0.2Fe0.8O3−δ air electrode–electrolyte interface on the short-term stability under high-current electrolysis in solid oxide electrolyzer cells. Journal of Power Sources. 2018;378:571-8.

[29] Xu H, Cheng K, Chen M, Zhang L, Brodersen K, Du Y. Interdiffusion between gadolinia doped ceria and yttria stabilized zirconia in solid oxide fuel cells: Experimental investigation and kinetic modeling. Journal of Power Sources. 2019;441:227152.

[30] Shen J, Miao B, Liu Q, Wu Y, Chan SH, Zhong Z, Pan Z. Activation of LSCF–YSZ interface by cobalt migration during electrolysis operation in solid oxide electrolysis cells. International Journal of Hydrogen Energy. 2022;47:38114-23.

[31] Kim J, Ji H-I, Dasari HP, Shin D, Song H, Lee J-H, et al. Degradation mechanism of electrolyte and air electrode in solid oxide electrolysis cells operating at high polarization. International Journal of Hydrogen Energy. 2013;38:1225-35.

[32] Hauch A, Ebbesen S, Jensen SH, Mogensen M. Solid oxide electrolysis cells: microstructure and degradation of the Ni/yttria-stabilized zirconia electrode. Journal of the Electrochemical Society. 2008;155:B1184.

[33] Chen M, Liu Y-L, Bentzen JJ, Zhang W, Sun X, Hauch A, et al. Microstructural degradation of Ni/YSZ electrodes in solid oxide electrolysis cells under high current. Journal of The Electrochemical Society. 2013;160:F883.

[34] Shang Y, Smitshuysen AL, Yu M, Liu Y, Tong X, Jørgensen PS, et al. 3D microstructural characterization of Ni/yttria-stabilized zirconia electrodes during long-term CO 2 electrolysis. Journal of Materials Chemistry A. 2023;11:12245-57.

[35] Wang Y, Banerjee A, Deutschmann O. Dynamic behavior and control strategy study of CO2/H2O co-electrolysis in solid oxide electrolysis cells. Journal of Power Sources. 2019;412:255-64.

[36] Rao M, Sun X, Hagen A. Durability of solid oxide electrolysis stack under dynamic load cycling for syngas production. Journal of Power Sources. 2020;451:227781.

[37] Sun A, Shuai W, Zheng N, Han Y, Xiao G, Ni M, Xu H. Self-adaptive heat management of solid oxide electrolyzer cell under fluctuating power supply. Energy Conversion and Management. 2022;271:116310.

[38] Zhu Z, Hu B, Tucker MC. Dynamic operation of metal-supported solid oxide electrolysis cells. International Journal of Hydrogen Energy. 2024;59:316-21.

[39] Tucker MC. Durability of symmetric-structured metal-supported solid oxide fuel cells. Journal of Power Sources. 2017;369:6-12.

[40] Tucker MC. Dynamic-temperature operation of metal-supported solid oxide fuel cells. Journal of Power Sources. 2018;395:314-7.

[41] Petipas F, Fu Q, Brisse A, Bouallou C. Transient operation of a solid oxide electrolysis cell. International journal of hydrogen energy. 2013;38:2957-64.

[42] Kaur G, Kulkarni AP, Giddey S. CO2 reduction in a solid oxide electrolysis cell with a ceramic composite cathode: effect of load and thermal cycling. International Journal of Hydrogen Energy. 2018;43:21769-76.

[43] Santhanam S, Padinjarethil A, Tomberg M, Heddrich MP, Ansar A. Transient operation strategies for MW-scale SOC systems. ECS Transactions. 2019;91:2571.

[44] Schefold J, Brisse A, Surrey A, Walter C. 80,000 current on/off cycles in a one year long steam electrolysis test with a solid oxide cell. International Journal of Hydrogen Energy. 2020;45:5143-54.

[45] Hartvigsen J, Kane N, Casteel M, Gomez J, Priest C, Wang L, et al. Development of Long Duration Button Cell Test Stands and Testing Protocols. ECS Transactions. 2023;111:1761.

[46] Shen F, Welander MM, Tucker MC. Metal-supported solid oxide electrolysis cell test standard operating procedure. Frontiers in Energy Research. 2022;10:817981.

[47] Coelho AA. TOPAS and TOPAS-Academic: an optimization program integrating computer algebra and crystallographic objects written in C++. Journal of Applied Crystallography. 2018;51:210-8.

[48] Bailey J, Heenan T, Finegan D, Lu X, Daemi S, Iacoviello F, et al. Laser-preparation of geometrically optimised samples for X-ray nano-CT. Journal of microscopy. 2017;267:384-96.

[49] Epting WK, Mansley Z, Menasche DB, Kenesei P, Suter RM, Gerdes K, et al. Quantifying intermediate-frequency heterogeneities of SOFC electrodes using X-ray computed tomography. Journal of the American Ceramic Society. 2017;100:2232-42.

[50] Chen M, Sun X, Chatzichristodoulou C, Koch S, Hendriksen PV, Mogensen MB. Thermoneutral operation of solid oxide electrolysis cells in potentiostatic mode. ECS Transactions. 2017;78:3077.

[51] Min G, Choi S, Hong J. A review of solid oxide steam-electrolysis cell systems: Thermodynamics and thermal integration. Applied Energy. 2022;328:120145.

[52] Schouler E, Kleitz M, Forest E, Fernandez E, Fabry P. Overpotential of H2-H2O, Ni/YSZ electrodes in steam electrolyzers. Solid State Ionics. 1981;5:559-62.

[53] Laguna-Bercero M, Campana R, Larrea A, Kilner J, Orera V. Electrolyte degradation in anode supported microtubular yttria stabilized zirconia-based solid oxide steam electrolysis cells at high voltages of operation. Journal of Power Sources. 2011;196:8942-7.

[54] Hauch A, Pylypko S, Cubizolles G, Mouginn J. Load cycling tests of reversible solid oxide cells–effects of current density, steam content, and utilization. ECS Transactions. 2021;103:437.

[55] Monaco F, Ferreira-Sanchez D, Hubert M, Morel B, Montinaro D, Grolimund D, Laurencin J. Oxygen electrode degradation in solid oxide cells operating in electrolysis and fuel cell modes: LSCF destabilization and interdiffusion at the electrode/electrolyte interface. International Journal of Hydrogen Energy. 2021;46:31533-49.

[56] Rowberg AJ, Slomski HS, Kim N, Strange NA, Gorman BP, Shulda S, et al. Impact of Sr-Containing Secondary Phases on Oxide Conductivity in Solid-Oxide Electrolyzer Cells. Chemistry of Materials. 2024.

[57] Jeffrey C, Develos-Bagarinao K, Ishiyama T, Kishimoto H, Yamaji K, Horita T, Yokokawa H. Elucidating the degradation mechanism at the cathode-interlayer interfaces of solid oxide fuel cells. Journal of The Electrochemical Society. 2018;165:F1340.

[58] Laurencin J, Hubert M, Sanchez DF, Pylypko S, Morales M, Morata A, et al. Degradation mechanism of La0.6Sr0.4Co0.2Fe0.8O3-δ/Gd0.1Ce0.9O2-δ composite electrode operated under solid oxide electrolysis and fuel cell conditions. Electrochimica Acta. 2017;241:459-76.

[59] Railsback J, Choi SH, Barnett SA. Effectiveness of dense Gd-doped ceria barrier layers for (La,Sr)(Co,Fe)O3 cathodes on Yttria-stabilized zirconia electrolytes. Solid State Ionics. 2019;335:74-81.

[60] Nechache A, Boukamp BA, Cassir M, Ringuedé A. Accelerated degradation of yttria stabilized zirconia electrolyte during high-temperature water electrolysis. Journal of Solid State Electrochemistry. 2019;23:871-81.

[61] Bernadet L, Segura-Ruiz J, Yedra L, Estrade S, Peiró F, Montinaro D, et al. Enhanced diffusion barrier layers for avoiding degradation in SOFCs aged for 14000 h during 2 years. Journal of Power Sources. 2023;555:232400.

[62] Jayapragasam P, Wen Y, Cook K, Wrubel JA, Ma Z, Huang K, Jin X. Crack Growth Rate at Oxygen Electrode/Electrolyte Interface in Solid Oxide Electrolysis Cells Predicted by Experiment Coupled Multiphysics Modeling. Journal of the Electrochemical Society. 2023;170:054509.

[63] Laguna-Bercero MA, Campana R, Larrea A, Kilner JA, Orera VM. Electrolyte degradation in anode supported microtubular yttria stabilized zirconia-based solid oxide steam electrolysis cells at high voltages of operation. Journal of Power Sources. 2011;196:8942-7.

[64] Tai LW, Nasrallah MM, Anderson HU, Sparlin DM, Sehlin SR. Structure and electrical properties of La1 − xSrxCo1 − yFeyO3. Part 2. The system La1 − xSrxCo0.2Fe0.8O3. Solid State Ionics. 1995;76:273-83.

[65] Slomski HS, Kaufman JL, Dzara MJ, Strange NA, Priest C, Hartvigsen JL, et al. Understanding (La, Sr)(Co, Fe) O3− δ Phase Instability within SOECs Using a Combined Experimental and Atomistic Modeling Approach. ACS Physical Chemistry Au. 2025.

[66] Shimura T, Miyazaki Y, Nakayama Y, Takeguchi M, Shikazono N. Characterization of inter-diffusion phase between gadolinium-doped ceria and yttria-stabilized zirconia during high-temperature sintering by in-situ and ex-situ transmission electron microscopy observations. Solid State Ionics. 2019;342:115058.

[67] Zhang Q, Park B-K, Barnett S, Voorhees P. On the role of the zirconia/ceria interface in the degradation of solid oxide electrolysis cells. Applied Physics Letters. 2020;117.

[68] da Costa Almeida PM. Formation of lanthanum zirconates in solid oxide electrolysis cells: experimental studies.

[69] Priest CM, Gomez JY, Kane NJ, Hartvigsen JL, Wang L, Ding D, et al. Challenges in practical button cell testing for hydrogen production from high temperature electrolysis of water. Frontiers in Energy Research. 2023;11:1278203.

[70] Schäfer D, Queda L, Nischwitz V, Fang Q, Blum L. Origin of Steam Contaminants and Degradation of Solid-Oxide Electrolysis Stacks. Processes. 2022;10:598.

[71] Mogensen MB, Chen M, Frandsen HL, Graves C, Hauch A, Hendriksen PV, et al. Ni migration in solid oxide cell electrodes: Review and revised hypothesis. Fuel Cells. 2021;21:415-29.

[72] Trini M, Hauch A, De Angelis S, Tong X, Hendriksen PV, Chen M. Comparison of microstructural evolution of fuel electrodes in solid oxide fuel cells and electrolysis cells. Journal of Power Sources. 2020;450:227599.

[73] Lay-Grindler E, Laurencin J, Villanova J, Cloetens P, Bleuet P, Mansuy A, et al. Degradation study by 3D reconstruction of a nickel–yttria stabilized zirconia cathode after high temperature steam electrolysis operation. Journal of Power Sources. 2014;269:927-36.

[74] Shearing PR, Bradley RS, Gelb J, Tariq F, Withers PJ, Brandon NP. Exploring microstructural changes associated with oxidation in Ni–YSZ SOFC electrodes using high resolution X-ray computed tomography. Solid State Ionics. 2012;216:69-72.

[75] Zhang Y, Yan F, Yan M, Wan Y, Jiao Z, Xia C, et al. High-throughput, super-resolution 3D reconstruction of nano-structured solid oxide fuel cell electrodes and quantification of microstructure-property relationships. Journal of Power Sources. 2019;427:112-9.

[76] Nelson GJ, Grew KN, Izzo JR, Lombardo JJ, Harris WM, Faes A, et al. Three-dimensional microstructural changes in the Ni–YSZ solid oxide fuel cell anode during operation. Acta Materialia. 2012;60:3491-500.

[77] Trini M, Jørgensen PS, Hauch A, Bentzen J, Hendriksen P, Chen M. 3D microstructural characterization of Ni/YSZ electrodes exposed to 1 year of electrolysis testing. Journal of The Electrochemical Society. 2019;166:F158.

[78] Mahbub R, Epting WK, Hsu T, Mason JH, Feng M, Nuhfer NT, et al. Quantitative analysis of multi-scale heterogeneities in complex electrode microstructures. Journal of The Electrochemical Society. 2019;167:054506.

[79] Bertei A, Ruiz-Trejo E, Kareh K, Yufit V, Wang X, Tariq F, Brandon N. The fractal nature of the three-phase boundary: a heuristic approach to the degradation of nanostructured solid oxide fuel cell anodes. Nano Energy. 2017;38:526-36.

[80] Mogensen MB, Hauch A, Sun X, Chen M, Tao Y, Ebbesen SD, et al. Relation between Ni particle shape change and Ni migration in Ni–YSZ electrodes–a hypothesis. Fuel cells. 2017;17:434-41.